Numerical simulation of magnetohydrodynamic flow in a toroidal duct of square cross-section

S. Vantieghem*

B. Knaepen

Statistical and Plasma Physics, Université Libre de Bruxelles, Campus Plaine, CP 231, B-1050 Brussels, Belgium

Abstract

We present numerical simulation results of the quasi-static magnetohydrodynamic (MHD) flow in a toroidal duct of square cross-section with insulating Hartmann walls and conducting side walls. Both laminar and turbulent flows are considered. In the case of steady flows, we present a comprehensive analysis of the secondary flow. It consists of two counter-rotating vortex cells, with additional side wall vortices emerging at sufficiently high Hartmann number. Our results agree well with existing asymptotic analysis. In the turbulent regime, we make a comparison between hydrodynamic and MHD flows. We find that the curvature induces an asymmetry between the inner and outer side of the duct, with higher turbulence intensities occurring at the outer side wall. The magnetic field is seen to stabilize the flow so that only the outer side layer remains unstable. These features are illustrated both by a study of statistically averaged quantities and by a visualization of (instantaneous) coherent vortices.

Key words: Magnetohydrodynamics, Curved duct

*Corresponding author Tel: +32 2650 58 23, stvtiegh@ulb.ac.be

Numerical simulation of magnetohydrodynamic flow in a toroidal duct of square cross-section

S. Vantieghem*

B. Knaepen

Statistical and Plasma Physics, Université Libre de Bruxelles, Campus Plaine, CP 231, B-1050 Brussels, Belgium

1. Introduction

In magnetohydrodynamics (MHD), one studies the coupling between flows of electrically conducting fluids and electromagnetic fields. This branch of physics describes a vast range of phenomena, like the origin of the Earth's magnetic field or the suppression of turbulence due to a magnetic field in industrial melt flows. For most industrial applications and laboratory flows, the coupling is virtually one-way; this means that the flow is significantly affected by the Lorentz force due to the action of the magnetic field, but that the induced magnetic field remains negligible compared to the externally imposed one. Such a behavior is the signature of flows in which the magnetic Reynolds number $R_m = \mu\sigma UL$ is small compared to one. Here, μ and σ are respectively the magnetic permeability and the electrical conductivity of the fluid, while U and L are typical velocity and length scales of the flow under consideration.

Under such conditions, called the quasi-static regime, the magnetic field

*Corresponding author Tel: +32 2650 58 23, stvtiegh@ulb.ac.be

mostly tends to suppress variations along its direction. If the magnetic field intensity is high, this results in a flow consisting of an extended, quasi-uniform core, surrounded by thin shear layers due to the presence of solid boundaries or discontinuities. We can distinguish between two different types of wall shear layers: the *Hartmann layer*, which occurs at walls with their normal vector non-perpendicular to the magnetic field and the *side layer* (or *parallel layer*), which emerges at walls parallel to the magnetic field. Under laminar conditions, their thickness can be expressed in terms of the Hartmann number M, a dimensionless measure of the ratio between the Lorentz and viscous force. The Hartmann layer has a typical thickness of $\mathcal{O}(M^{-1})$, while that of the side layer scales as $\mathcal{O}(M^{-1/2})$. These shear layers are prone to three-dimensional stabilities, as discussed by Thess and Zikanov (2007).

In the past years, there has been considerable interest in the role of the different shear layers in the transition of wall-bounded MHD shear flows. Krasnov et al. (2004) performed a computational study of the instability of the Hartmann layer, and found that the parameter which governs the transition, is the ratio between the Reynolds number Re and the Hartmann number. In their study, the transition is seen to occur for values of Re/M between 350 and 400. Moresco and Alboussière (2004) performed friction factor measurements in a toroidal duct of square cross-section at high Hartmann and Reynolds number. Since the major part of the friction occurs in the Hartmann layer for high Hartmann number flows, they conjectured that a sudden change in the behavior of the friction factor is related to a transition in the Hartmann layer. Their measurements showed that this transition occurs at $Re/M \approx 380$, regardless of the exact value of the Hartmann number. A linear stability analysis of Lingwood and Alboussière (1999) yielded

a critical value of $Re/M \approx 48250$. This large discrepancy indicates that the transition is triggered by nonlinear effects.

The experimental method adopted in Moresco and Alboussière (2004) did however not allow to study the behavior of the side layers. A computational study of Krasnov et al. (2010) on the other hand, showed that the nuclei of instability in MHD straight duct flow are located in the side layers. The common feature in all these studies is that the Hartmann walls are insulating. Other authors have considered the instability in duct flows with conducting Hartmann walls (Reed and Picologlou, 1989; Kinet et al., 2009). These flows however are characterized by strong side wall jets, and undergo a completely different transition; they are not directly relevant to the present work.

It is clear that the experiment of Moresco and Alboussière (2004) is far from fully understood. Currently, it is unfortunately not possible to access the whole parameter range covered in the experiment with numerical simulations. Moreover, even the laminar behavior of MHD toroidal duct flow is relatively unexplored. To the best of our knowledge, only two studies of the laminar flow in such a configuration have been undertaken. The first one was performed by Baylis and Hunt (1971). They used an asymptotic approach, i.e. they assumed the existence of an inertialess and inviscid core, which is surrounded by thin shear layers. Their results show that the inertial term is negligible when the aspect ratio between the length and the average radius R of the duct is small compared to M/R. One decade later, Tabeling and Chabrerie (1981) performed a more detailed analysis, in which they considered the curvature as a small parameter. This allowed them to compute the secondary flow profile in the shear layers for sufficiently low values of the curvature and the Reynolds number and high values of the Hartmann num-

ber. They predicted that streamwise-oriented vortices would occur in the parallel layers, whose exact shape depends on the electric boundary conditions. Furthermore, they found that the secondary flow has a strong radially inward component along the Hartmann layers.

Hence, the aim of this work is to compute the full solution the MHD flow of a liquid metal in a toroidal duct. Our work is organized as follows: first, we outline the mathematical formulation and the computational details of our simulations. The two following sections are devoted to a discussion of the results for respectively steady and non-steady flows. The last section summarizes the most important conclusions of this work.

2. Mathematical model and computational method

We consider the incompressible flow, characterized by a velocity field $\mathbf{u}$, of a fluid in a square annular duct with mean radius R and length $2L$ (see figure 1). The axis of the torus is along the y-direction. The material properties of the fluid, like its mass density ρ, kinematic viscosity ν and electrical conductivity σ are assumed to be constant. The flow is subjected to a uniform magnetic field $\mathbf{B} = B_0\mathbf{1}_y$. Moreover, we assume that the magnetic Reynolds $R_m \ll 1$, so that the magnetic field does not change with time; this is called the quasi-static approximation. This means that the induced electric field can be derived from a scalar potential function ϕ (Roberts, 1967). The electric current density $\mathbf{j}$ obeys Ohm's law for a moving conductor:

$$\mathbf{j} = \sigma\left(-\nabla\phi + \mathbf{u}\times\mathbf{B}\right) \tag{1}$$

The constraint of charge conservation under the quasi-neutrality assumption, $\nabla \cdot \mathbf{j} = 0$, leads to a Poisson equation for the potential:

$$\nabla^2 \phi = \nabla \cdot (\mathbf{u} \times \mathbf{B}) \tag{2}$$

The equations of mass and momentum conservation are the standard incompressible Navier-Stokes equations in which a Lorentz force term is added:

$$\rho \left(\partial_t \mathbf{u} + \mathbf{u} \cdot \nabla \mathbf{u} \right) = -\nabla p + \rho \nu \nabla^2 \mathbf{u} + \mathbf{j} \times \mathbf{B} \tag{3}$$

$$\nabla \cdot \mathbf{u} = 0 \tag{4}$$

The boundary conditions for $\mathbf{u}$ and ϕ are the following. For the velocity, we apply standard no-slip conditions on all the walls. The electrical boundary conditions are inspired by the work of Moresco and Alboussière (2004). This means that we have perfectly insulating Hartmann walls and perfectly conducting side walls. Mathematically:

$$\mathbf{u} = 0, \partial_n \phi = 0 \quad \text{at} \quad y = \pm L \tag{5}$$

$$\mathbf{u} = 0, \phi = \pm V/2 \quad \text{at} \quad r = R \pm L \tag{6}$$

This makes clear why we don't need an external forcing term in equation (3). By imposing a voltage difference between the side walls, a radial current is injected in the fluid. The Lorentz force resulting from the interaction between this current and the magnetic field, provides the necessary forcing of the flow. Our formulation is slightly different from the one of Moresco and Alboussière (2004) in the sense that, in the experiment, the amount of injected current at the side walls was fixed, rather then the potential. In other words: The side wall potential in the experiment was thus constant in space, but still varying in time, while we allow fluctuations in time of the total amount of injected current. In the laminar regime, both formulations

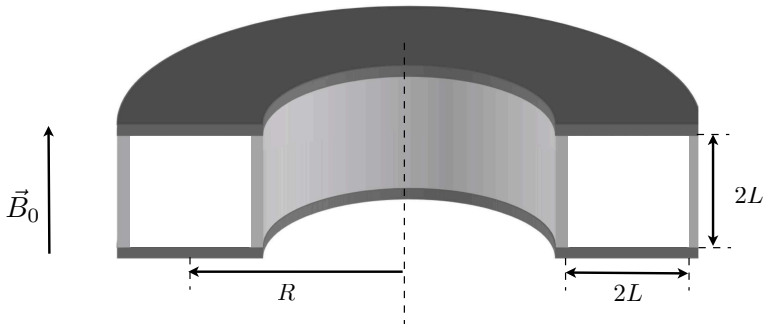

Figure 1: Sketch of the annular geometry. The color of the walls indicates their electric conductivity: perfectly conducting (light grey), and perfectly insulating (dark grey).

are of course strictly equivalent.

We can use the linearity of the Laplacian operator to split equation (2) with boundary conditions (5-6) in two parts: $\phi = \phi_1 + \phi_2$. Here, ϕ_1 is a solution of the non-homogeneous equation (2) with Neumann conditions on the Hartmann walls and homogeneous Dirichlet conditions $\phi_1 = 0$ on the side walls. ϕ_2 on the other hand is a solution of the Laplace equation $\nabla^2\phi_2 = 0$, also with Neumann conditions, but now with non-homogeneous Dirichlet conditions $\phi_2 = \pm V/2$ at $r = R \pm L$. In the present geometry, the potential ϕ_2 and the corresponding external forcing $\mathbf{f}_{ext}$ take the following form:

$$\phi_2 = \frac{V}{\ln\left(\frac{R+L}{R-L}\right)} \ln\left(\frac{r}{\sqrt{R^2 - L^2}}\right) \tag{7}$$

$$\mathbf{f}_{ext} = -\sigma \nabla\phi_2 \times \mathbf{B} = f_{ext}\mathbf{1}_\theta = \frac{VB}{r \ln\left(\frac{R+L}{R-L}\right)}\mathbf{1}_\theta \tag{8}$$

We see that $\nabla\phi_2$, and thus the external forcing, decrease as $1/r$ in radial direction and are independent of the velocity field.

The different cases that we will consider can be characterized by three non-

dimensional numbers: the well-known Reynolds number Re, the Hartmann number M, and the ratio between the duct length and the mean radius of the annulus:

$$Re = \frac{UL}{\nu} \tag{9}$$

$$M = B_0 L \sqrt{\frac{\sigma}{\rho\nu}} \tag{10}$$

$$\zeta = \frac{L}{R} \tag{11}$$

In the definition of Re, the characteristic velocity U is defined as the bulk streamwise velocity. We use a finite-volume method to discretize the equations. Our code is called YALES2, and is discussed in Moureau et al. (2011). All the variables are defined at the centers of the control volumes. It is however necessary to define velocities at the control volume faces to avoid spurious pressure oscillations. The spatial discretization is based on a central-difference-like stencil. For the time-stepping algorithm, we apply a canonical fractional-step method (Kim and Moin, 1985) with a Crank-Nicholson time discretization for the viscous term, and a semi-implicit treatment for the non-linear term; this means that we use a Crank-Nicholson discretization for the convected velocity and an Adams-Bashforth method for the convecting velocity. As such, the system of equations resulting from the implicit treatment is linear.

The Lorentz force is treated explicitly, to avoid a coupling between the Poisson equation for the potential and the advancement of the velocity field. The computation of the Lorentz force is carried out with a so-called current conservative method (Ni et al., 2007a,b), i.e. the current is computed as a divergence:

$$\mathbf{j} = \nabla \cdot (\mathbf{jr}) \tag{12}$$

This formulation reduces the total current in the domain to a boundary term, and thus avoids global spurious contributions to the Lorentz force due to discretisation errors. The Poisson equations for both the potential and the pressure are solved with an algebraic multigrid method.

3. Laminar flow

In the present work, we extend the results of Tabeling and Chabrerie (1981) to more modest values of M and larger values of ζ or Re. We consider the following parameter combinations $M = 25$, 100 or 400, $Re \approx 0$, 100 or 800, and $\zeta = 1/9$. For all these cases, we assume that there exists a solution which is independent of time and the polar coordinate θ. This allows us to simulate only a small section of the torus. This assumption has been verified for the parameter combination $M = 25$ and $Re \approx 800$. We performed a simulation in a complete torus (512 points in streamwise direction, and 100 in both y- and r-direction) with a random velocity field as initial condition. It appears that the final state eventually becomes independent of time and of the streamwise coordinate, at least up to the accuracy threshold of the iterative solvers. For the other parameter combinations, we did not perform this check, and can not formally exclude that the flow has a three-dimensional character. Our assumption of two-dimensionality for these parameter combinations is then based on the following argument. According to Baylis and Hunt (1971), the importance of the non-linear term in the momentum balance, which triggers three-dimensional effects, becomes smaller if the value of $\xi^2 \times (Re^2/M^4)$ decreases. For all investigated values of Re and M, the combination $M = 25$, $Re \approx 800$ yields the highest value of $\xi^2 \times (Re^2/M^4)$. For this parameter combination, we have numerical evi-

dence that the flow is independent of the azimuthal coordinate θ. As such, we do not expect three-dimensional effects to occur for the other parameter combinations investigated.

The results that we present here, are thus obtained by simulating a section of 0.216 radials (12.5 degrees) and 32 grid points in streamwise direction. As such, we can increase the resolution in both y- and r-direction to 192 points. The grid is stretched in the core regions, according to a tangent hyperbolic profile, so that we can resolve the Hartmann and side layers with more details. These layers contain respectively 6 and 10 equidistant points in wall normal-directions. The parameters of the tanh-stretching are chosen such that the grid spacing transitions smoothly between the boundary layer region and core regions. A cross-section of the mesh along two intersection planes is shown in figure 2. The simulation for which $Re = 0$ is obtained by omitting the non-linear term. Figure 3 shows the non-dimensionalized product of the radial coordinate and streamwise velocity profile along the centerline of the duct in the radial direction: $u_\theta r(U_0 R)^{-1}$. In the previous expression, the reference centerline velocity U_0 is defined as:

$$U_0 = \frac{V}{B_0 R \log\left(\frac{R+L}{R-L}\right)} \tag{13}$$

As expected, we see that the velocity in the core becomes more and more uniform as M increases. The results also illustrate that the velocity scales, up to the leading order in M, as $f_{ext} M^{-2} \propto V/B$. This is in agreement with the asymptotic analysis of Hunt and Stewartson (1965).

When the Hartmann number is high, the only relevant force in the core is the Lorentz force $j_r B_0$, and the effect of the curvature is a simple decrease of the streamwise velocity in the radial direction, a reflection of the $1/r$ behavior of the 'external forcing' as discussed in the previous section. This

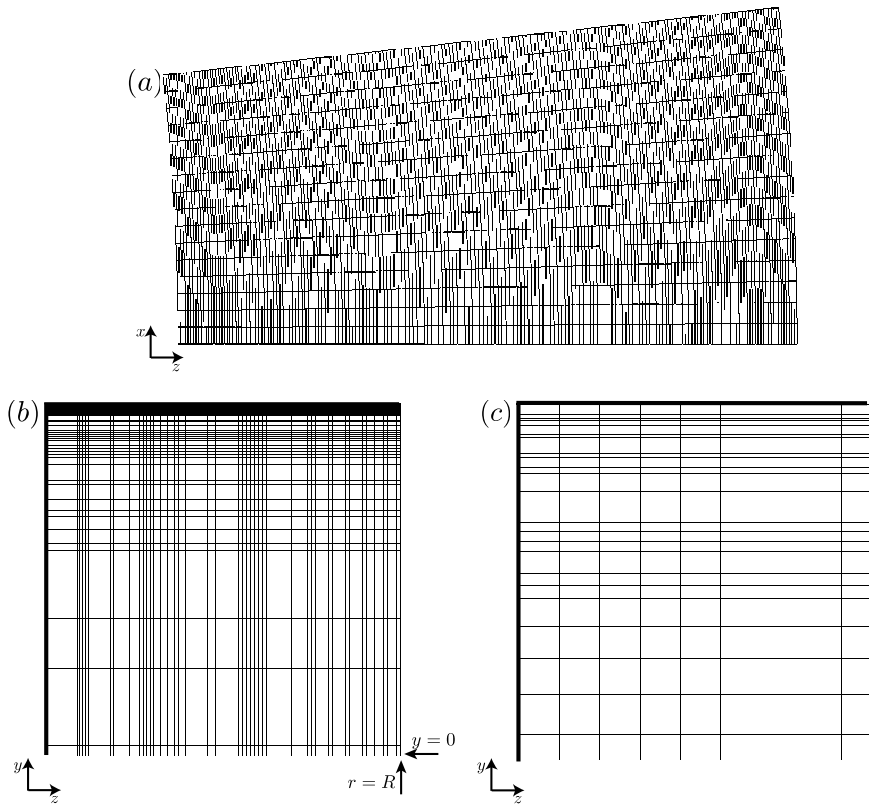

Figure 2: Grid lines of the mesh used to simulate the laminar flow at $M = 400$ in a cross-section along the plane $y = 0$ (a) and a quarter cross-section along the plane $x = 0$ ($z = r < R$ and $y > 0$) (b). Detail of the mesh in the plane $x = 0$ near the corner between the Hartmann and side wall (c).

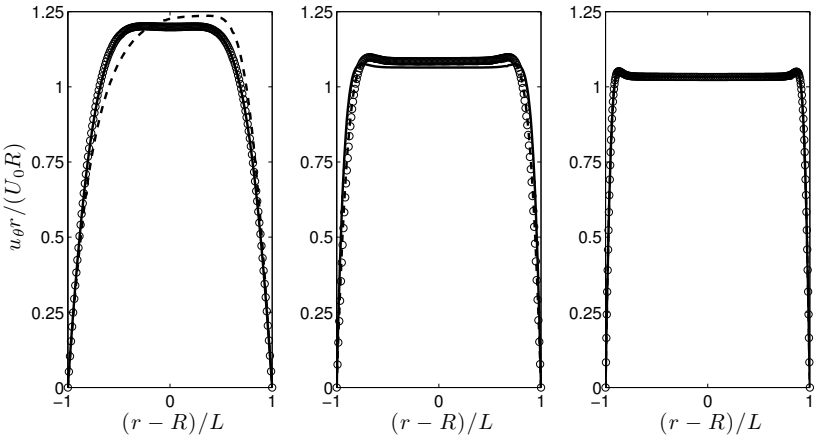

Figure 3: Streamwise velocity profiles for different Reynolds and Hartmann numbers along the radial centerline of the duct. $M = 25$ (left), $M = 100$ (center), $M = 400$ (right), and $Re = 0$ $(-)$, $Re \approx 100$ $(--)$ and $Re \approx 800$ $(\circ)$.

is clear from figure 3, where we have a uniform profile of $u(r, y = 0)r$ along the radial centerline in the core, with minor overspeed zones in the side layers; these zones exist also in the limit of $R \to \infty$, i.e. in a straight, square duct. At lower Hartmann number ($M = 25$), inertia starts to play a role. A useful parameter in this context is the interaction parameter N, an estimate of the ratio between the Lorentz force and inertia, defined as $N = M^2/Re$. This parameter becomes of order one for $M = 25$ and $Re \approx 800$. In that case, the streamwise velocity is 'pushed' towards the exterior wall. At higher Hartmann number, the profiles for different values of Re are virtually identical.

In figure 4, we show the streamwise velocity distribution along the magnetic field direction, close to the upper wall at $y = L$ (i.e. in the vicinity of one of the Hartmann layers), for different values of r. The results are shown

together with the analytical Hartmann profile $u_{Ha,an}$ defined as:

$$u_{Ha,an} = u(y = 0, r = R)\left(1 - \exp\left(-ML^{-1}(1 - y)\right)\right) \tag{14}$$

For $M = 100$ and $M = 400$, we observe that the numerical velocity profiles agree very well with the analytical one. If $M = 25$ on the other hand, this agreement is only satisfactory for the results along the line $r = R$. For this value of the Hartmann number however, the positions $r = R \pm 0.5L$ may be located in the side layers. As such, it should not be expected that the velocity distribution at these positions tends towards the analytical Hartmann profile. Finally, for $Re \approx 800$, we see that the results at $r = R + 0.5L$ and $r = R - 0.5L$ do not collapse anymore; this asymmetry was already inferred from the results displayed in figure 3 (l.h.s.).

Since $\partial_\theta u_\theta = 0$ in the laminar case, the vector field $\mathbf{u}_s = u_y\mathbf{1}_y + u_r\mathbf{1}_r$ is a proper, solenoidal velocity field in two dimensions, and is termed secondary flow. In figure 5 (a), we display the magnitude of this secondary flow field in the complete cross-section of the torus, rescaled by U_0, i.e:

$$U_s(r, y) = U_0^{-1}\sqrt{v^2(r, y) + u_r^2(r, y)} \tag{15}$$

Figure 5 (b) shows the streamlines of the secondary flow. For axisymmetric flows, these can be computed as the isolines of a streamfunction ψ, which satisfies:

$$\frac{1}{r}\nabla\psi \times \mathbf{1}_\theta = \mathbf{u}_s \tag{16}$$

Component-wise, this reads:

$$u_r = -\frac{1}{r}\frac{\partial\psi}{\partial y} \tag{17}$$

$$u_y = \frac{1}{r}\frac{\partial\psi}{\partial r} \tag{18}$$

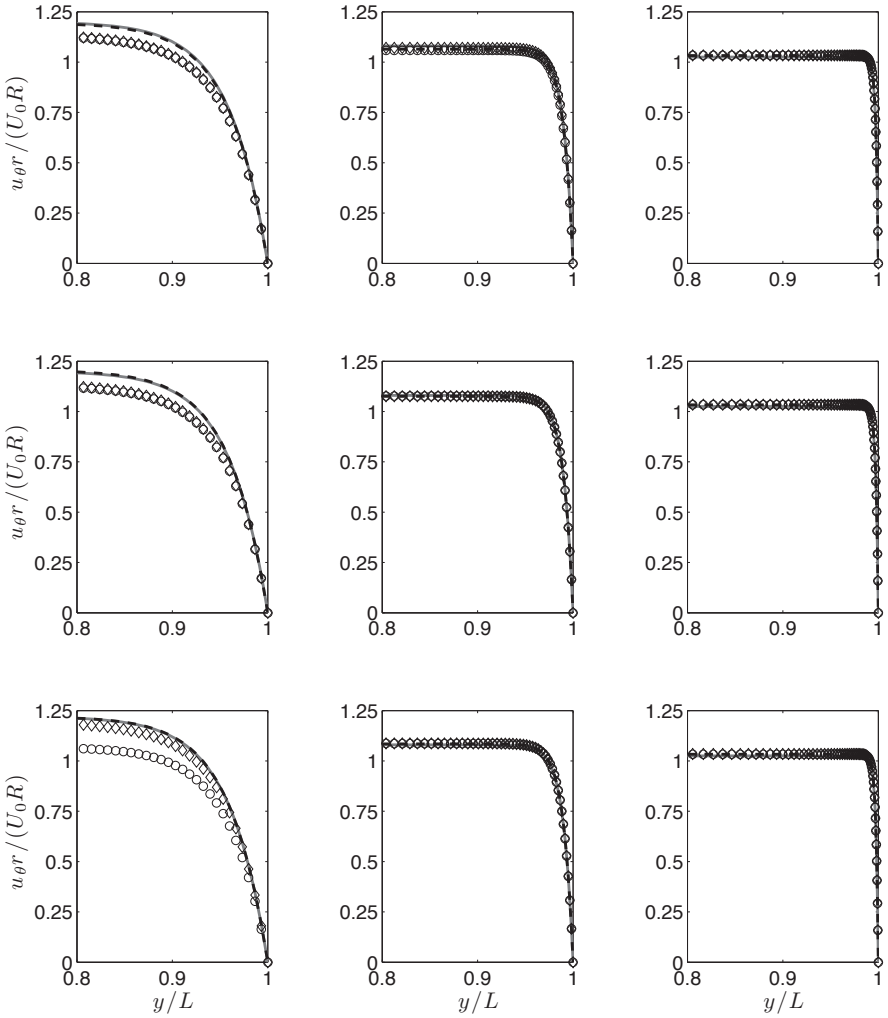

Figure 4: Streamwise velocity profiles along the magnetic field direction at various values of r for different Reynolds and Hartmann numbers along the radial centerline of the duct: $M = 25$ (left), $M = 100$ (center), $M = 400$ (right), and $Re = 0$ (top), $Re \approx 100$ (center), $Re \approx 800$ (bottom). Results at $r = R$ $(--)$, $r = R - 0.5L$ $(\circ)$, $r = R + 0.5L$ $(\diamond)$, and analytical profile (solid,grey).

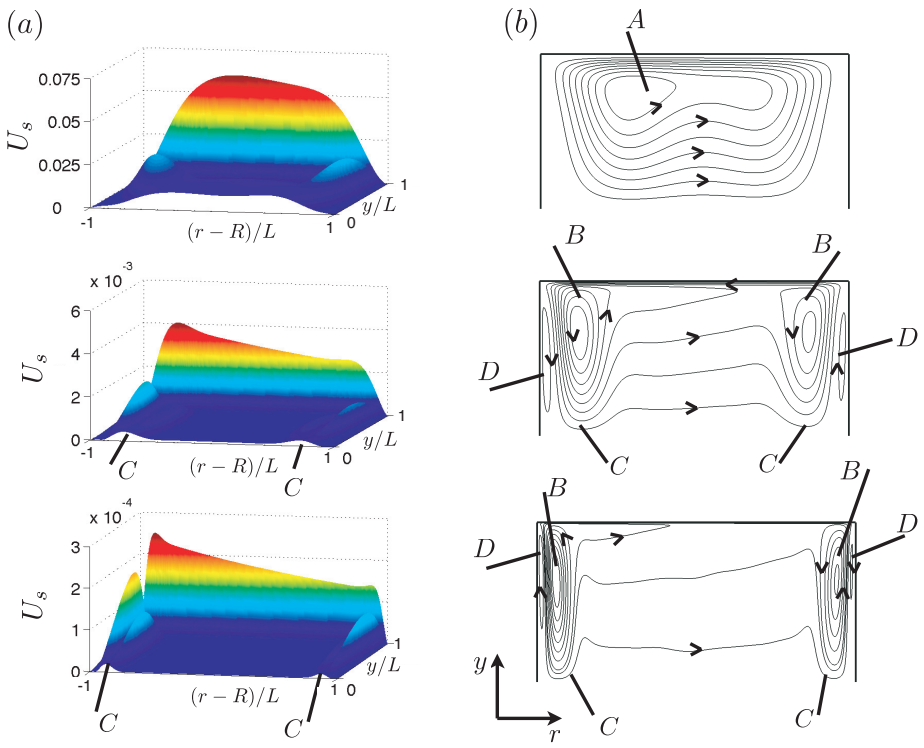

Figure 5: Secondary flow profile: magnitude U_s (a) and streamlines (b) for $Re \approx 100$, and for different values of the Hartmann number. $M = 25$ (top), $M = 100$ (center), $M = 400$ (bottom).

It follows that:

$$\frac{\partial^2 \psi}{\partial r^2} + \frac{\partial^2 \psi}{\partial y^2} = \frac{\partial}{\partial r}\left(r u_y\right) - \frac{\partial}{\partial y}\left(r u_r\right) \tag{19}$$

If we now define $\mathbf{u}'_s = u_y \mathbf{1}_r - u_r \mathbf{1}_y$, we can write (19) as:

$$\nabla^2 \psi = \nabla \cdot \left(r \mathbf{u}'_s\right) \tag{20}$$

in which r and y are to be considered as if they were cartesian variables. In order to compute ψ, we can proceed as follows: on a two-dimensional mesh which is an exact copy of the cut along planes $\theta = cst$ of the 3D mesh which was used to perform the simulations, (like the one shown in figure 2(b)) we compute the right-hand side of (20), and subsequently solve the Poisson equation (20). This equation is solved with Dirichlet conditions $\psi = 0$ on all the walls. We show only results in the upper half plane, since U_s and ψ are respectively symmetric and antisymmetric around the axis $y = 0$.

For $M = 25$, we see that we have one vortex cell, rotating in counterclockwise direction, with a stagnation point ('A' in figure 5 (b)) towards the inner wall. As the Hartmann number increases, the main vortex starts to develop two subvortices ('B' in figure 5 (b)) of unequal strength; the one at the inner side wall has a higher velocity than the one at the outer side wall. These subvortices exhibit a kind of 'bump' ('C' in figure 5 (b)) in the side layers: they have a large component in y-direction and then suddenly turn into the opposite direction. This bump reveals itself in the profile of U_s as a valley between two hills ('C' in figure 5 (a)). At last, for $M = 100$ and $M = 400$, we see the emergence of sidewall vortices, which are rotating in the clockwise direction ('D' in figure 5 (b)), as predicted by Tabeling and Chabrerie (1981). Due to their small spatial extent, it is difficult to discern them in figure 5. Therefore, we plot the details of U_s and ψ in the side wall regions in figure 6, in which the radial coordinate has been rescaled to units

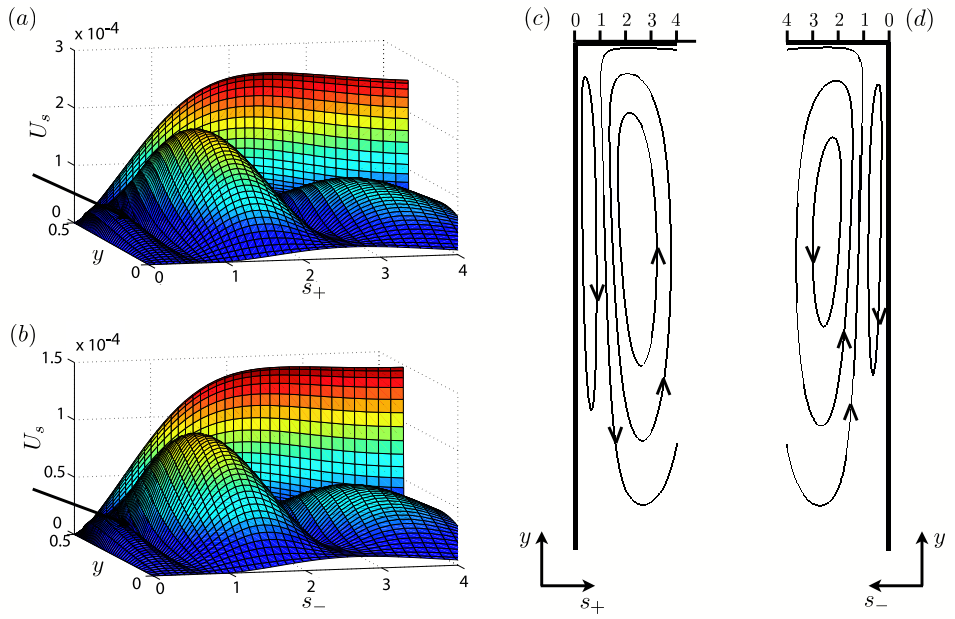

Figure 6: Detail of the secondary flow profile for $Re \approx 100$ and $M = 400$. Magnitude of the secondary flow at the inner (a) and outer (b) side wall; arrows indicate the location of side wall vortices. Streamlines at the inner (c) and outer (d) side wall.

of the side layer thickness: $s_\pm = \sqrt{M}(R \pm L \mp r)$; the location of the side wall vortices are indicated by arrows in figure 6 (a) and (b). These side wall vortices are much weaker than the main secondary flow vortex.

In figure 7, the radial velocity is plotted along the center line $r = R$ (i.e. along the direction of the magnetic field) in the vicinity of the Hartmann layer. The coordinate η is a rescaling of y with the Hartmann number and the duct length:

$$\eta = M\left(1 + \frac{y}{L}\right) \tag{21}$$

The velocity itself is rescaled as:

$$U_{rad}(\eta) = -M^2\left(\frac{\nu R}{L^2}\right) U_0^{-2} u_r(\eta, r = R) \tag{22}$$

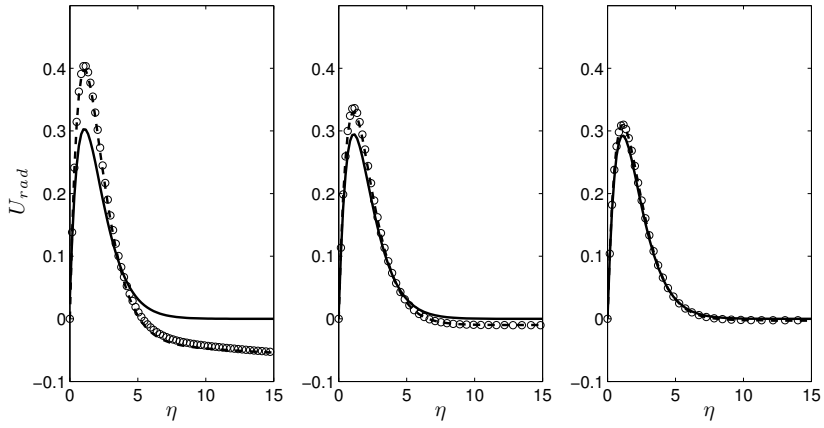

Figure 7: Radial velocity profiles in the Hartmann layer: Comparison between the asymptotic solution ($-$) and the numerical results for different values of the Reynolds and Hartmann number. $M = 25$ (left), $M = 100$ (center), $M = 400$ (right), $Re \approx 100$ ($--$) and $Re \approx 800$ ($\circ$).

and can be compared to its asymptotic counterpart in the Hartmann layer (Tabeling and Chabrerie, 1981):

$$\begin{aligned} U_{rad,as}(\eta) &= \frac{1}{6}\left[6\left(\eta - 1/3\right)\mathrm{e}^{-\eta} + 2\mathrm{e}^{-2\eta}\right] \\ &\quad + \frac{5}{6}M\mathrm{e}^{-\eta} + \mathcal{O}\left(M^{-3}\right) \end{aligned} \tag{23}$$

The simulation results only converge very slowly towards the asymptotic ones with increasing M. Even at $M = 400$, the difference between both results at the maximum of U_{rad} is still around six percent, and this is much larger than one would expect from a leading-error term of $\mathcal{O}(M^{-3})$. On the other hand, we see that the results for both values of Re almost collapse. The discrepancy between the asymptotic and numerical results might be explained by the fact that expression (23) represents only a first-order term in an expansion in ζ, and is only exact in the limit of $\zeta \to 0$. In the

present case, ζ takes the value of $1/9$, so that higher-order terms due to curvature-induced non-linearities, may still have a considerable influence. We finally note that the tendency of U_{rad} has the same order-of-magnitude for all combinations of Re and M. Given (22) and (23), it implies that u_r scales as $(U_0 M)^{-2}$.

4. Time-dependent flow

In this section, we compare the nature of the turbulence between the magnetohydrodynamic and hydrodynamic cases. Our main interest is in the level of turbulence in the different types of boundary layers. We consider three values of the Hartmann number: $M = 0, 10$ and 30. For the hydrodynamic case ($M = 0$), the flow is forced by a streamwise pressure gradient which is constant in time, and can be written as $\frac{1}{r}\frac{\partial P}{\partial \theta}$, with $\frac{\partial P}{\partial \theta}$ a constant. Note that this last case is not physical; the integral $\int_{\theta=0}^{2\pi} \frac{\partial P}{\partial \theta}\, \mathrm{d}\theta$ should be strictly zero since the pressure has a unique value at every point in space. On the other hand, the Navier-Stokes equations contain a pressure gradient term, but do not depend directly on the value of the pressure itself. Hence, this constraint is of no relevance for our computations.

To the best of our knowledge, no profound study of this hydrodynamic case has been performed until now. The Reynolds number in the three simulations is between 3900 and 4000. Furthermore, the duct side and the mean radius of the torus are chosen such that $\xi = 1/18 \approx 0.0555$. This section covers an angle of $\pi/4$ radials, which implies that the streamwise extent of the simulation domain is about seven times the distance between the duct walls. The mesh consists of 256 nodes in the streamwise direction and 100×100 nodes (along orthogonal grid lines) in the cross-section of the duct,

where a stretching was applied. In the hydrodynamic case, the stretching was such that the mesh contained at least three points within a distance of one (turbulent) boundary layer thickness δ of the walls. This length scale is given by the expression $\delta = \nu/u_\tau$ where the friction velocity u_τ can be defined as: $u_\tau^2 = -\frac{1}{2LR}\frac{\partial P}{\partial \theta}$. The quantity $\frac{1}{R}\frac{\partial P}{\partial \theta}$ represents the forcing at $r = R$. Strictly spoken, this last formula only holds in the limit $R \to \infty$ (straight duct flow driven by a uniform pressure gradient), but it should also provide an accurate estimate of the boundary layer thickness in the present case, given the rather small value of the curvature that is considered.

The same mesh is used for the case $M = 10$. For $M = 30$ however, a less severe stretching is applied in the Hartmann layers, since we presume that these layers would be stabilized due to the presence of the magnetic field. Statistics are obtained by a time averaging over, respectively, 720 ($M = 0$), 420 ($M = 10$) and 240 ($M = 30$) convective time scales L/U.

In figure 8 (above), we compare the main streamwise profile $\overline{u}_\theta$ for the different Hartmann numbers. Here, $\overline{u}_\theta$ denotes the average of u_θ over time and the azimuthal direction. In the case $M = 0$, we see that the centrifugal force shifts the velocity maximum towards the outer wall. For smaller values of r, the velocity maximum is not located on the symmetry axis $y = 0$, but close to the upper and lower wall. We find a similar profile for the case $M = 10$. The most striking tendency is that variations along the magnetic field direction tend to disappear in the case $M = 30$. Streamlines of the mean secondary flow are shown in figure 8 (below). These were computed with the same procedure as described above. We have again two counter-rotating vortex cells, whose stagnation points are now shifted towards the outer wall. For the case $M = 10$ this vortex pair is accompanied by a much weaker, counterrotating pair, located close to the outer side wall.

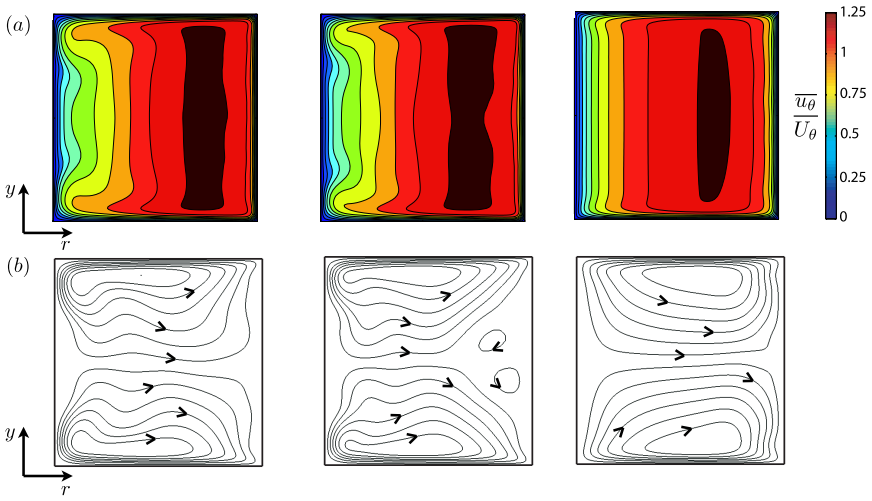

Figure 8: Isolines of the streamwise velocity (above) and streamlines of the secondary flow (below). Results for $M = 0$ (left), $M = 10$ (middle) and $M = 30$ (center).

In figure 9, we show isolines of the fluctuating streamwise velocity u_θ^{rms}, defined as:

$$u_\theta^{rms} = \sqrt{\overline{u_\theta u_\theta} - \overline{u_\theta}^2} \tag{24}$$

The magnitude of u_θ^{rms} can be interpreted as a measure for the turbulence intensity. In the hydrodynamic case ($M = 0$), we see that all shear layers are turbulent and that u_θ^{rms} takes a smaller, although non-negligible value in the core. Furthermore, there is an asymmetry between the inner and outer side wall. The turbulence is more intense at the outer side layer, in spite of the fact that the external force is the weakest in this region. This is in agreement with previous studies of curved channel flow (Moser and Moin, 1987; Nagata and Kasagi, 2004). As the Hartmann number increases, u_θ^{rms} is strongly suppressed in the core, the inner side layer and the Hartmann layers, whereas a significant level of turbulence persists in the outer side

layer. This illustrates that unstable side layers may exist in an otherwise stable flow.

These observations are confirmed by a visualization of coherent vortices in the flow. According to Jeong and Hussain (1995), such a vortex can be defined as a connected region in space with two negative eigenvalues of $C_{ik} = S_{ij}S_{jk} + \Omega_{ij}\Omega_{jk}$, with S_{ij} and Ω_{ij} being respectively the symmetric and anti-symmetric part of the velocity gradient tensor $\partial_i u_j$. In figure 10, we show the regions in the flow for which the second largest eigenvalue of C_{ik} is smaller then -0.08; this means that the weakest vortex cores (with a second eigenvalue between -0.08 and 0.0) are left away to not overload the figure. In the hydrodynamic case, we see that these structures are distributed over the complete flow domain, with a higher density of vortices in the vicinity of the outer wall. When a magnetic field is imposed, all these structures tend to be suppressed with exception of the ones close the outer wall. Furthermore, we observe that the structures become larger and populate less densely the flow as the magnetic field strength increases. A similar tendency was observed by Krasnov et al. (2008) in a numerical investigation of turbulent MHD channel flow with spanwise magnetic field. Contrary to other studies of MHD shear flows (Kinet et al., 2009), no elongation of these structures along the magnetic field direction is found. Probably the value of the interaction parameter $N \approx 0.2$ is too small for this to be observed.

5. Conclusions

In this work, we presented an analysis of the quasi-static MHD flow in a toroidal duct of square cross-section by means of numerical simulations. In the case of laminar flow, we saw that an increase of the external

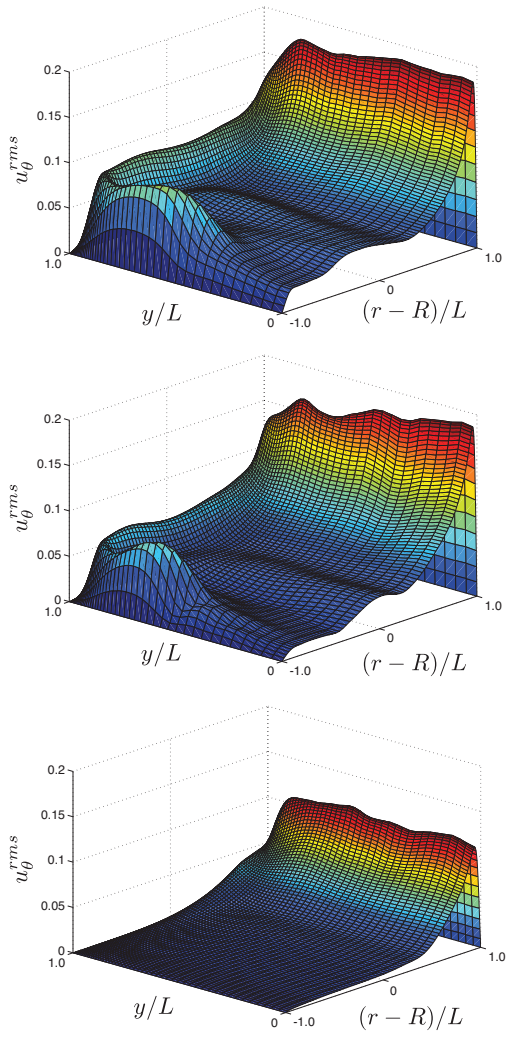

Figure 9: Statistics of the fluctuating streamwise velocity u_θ^{rms} for different values of the Hartmann number: $M = 0$ (above), $M = 10$ (center), $M = 30$ (below).

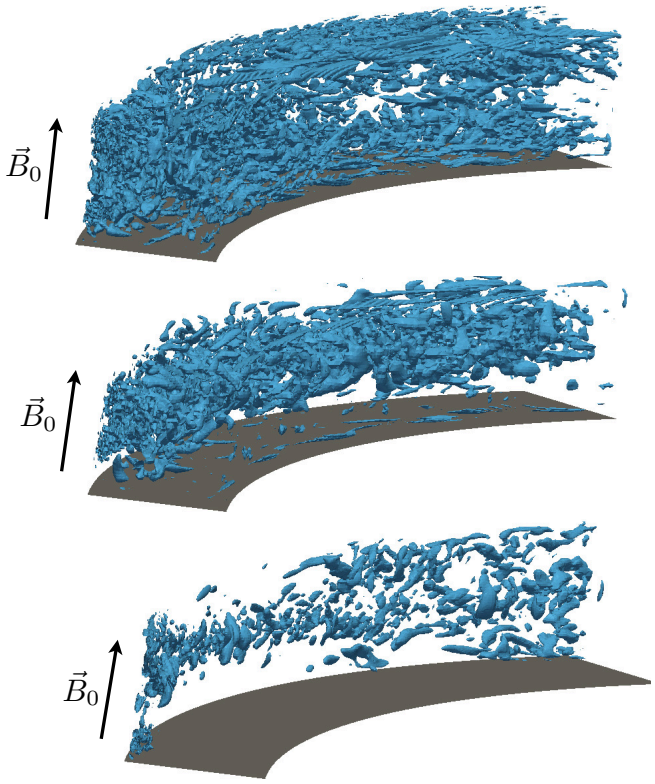

Figure 10: Coherent structures in the flow. Isosurfaces of the value of the second largest eigenvalue $\lambda_2 = -0.08$ of the tensor C_{ik}: $M = 0$ (above), $M = 10$ (center), $M = 30$ (below). The grey plane indicates the bottom wall of the torus.

magnetic field leads to a drastic change of the main and secondary flows; this secondary flow consists of two counter-rotating Ekman vortex cells, but also exhibits side layer vortices at high Hartmann number. Our results confirmed and extended the earlier asymptotic analysis of Tabeling and Chabrerie (1981). In the study of the turbulent regime, we found that the streamline curvature leads to an asymmetric level of turbulence at the convex and concave side walls. We also showed that a magnetic field suppresses turbulence in the core boundary layers. Moreover, we found that unstable side layers can coexist with stable Hartmann layers. At last, a study of coherent structures in the flow yielded an additional illustration of the main features of the turbulent regime.

Acknowledgements

We are grateful to T. Demaet, Y. Zhao and O. Zikanov for fruitful discussions, and to V. Moureau for providing the code which was used for this study.

This work, conducted as part of the award (Modelling and simulation of turbulent conductive flows in the limit of low magnetic Reynolds number) made under the European Heads of Research Councils and European Science Foundation EURYI (European Young Investigator) Awards scheme, was supported by funds from the Participating Organisations of EURYI and the EC Sixth Framework Programme. The content of the publication is the sole responsibility of the authors and it does not necessarily represent the views of the Commission or its services. The support of FRS-FNRS Belgium is also gratefully acknowledged.

References

Baylis, J. A., Hunt, J. C. R., 1971. MHD flow in an annular channel: theory and experiment. J. Fluid Mech. 3, 423–428.

Hunt, J. C. R., Stewartson, K., 1965. Magnetohydrodynamic flow in rectangular ducts. II. J. Fluid Mech. 23 (3), 563–581.

Jeong, J., Hussain, F., 1995. On the identification of a vortex. J. Fluid Mech. 285, 69–94.

Kim, J., Moin, P., 1985. Application of a fractional-step method to incompressible navier-stokes equations. J. Comp. Phys. 59, 308–323.

Kinet, M., Knaepen, B., Molokov, S., 2009. Instabilities and transition in magnetohydrodynamic flows in ducts with electrically conducting walls. Phys. Rev. Lett. 103 (15).

Krasnov, D. S., Zienicke, E., Zikanov, O., Boeck, T., Thess, A., 2004. Numerical study of the instability of the Hartmann layer. J. Fluid Mech. 504, 183–211.

Krasnov, D., Zienicke, E., Zikanov, O., Boeck, T., Thess, A., 2004. Numerical study of the instability of the Hartmann layer. J. Fluid Mech. 504, 183–211.

Krasnov, D., Zikanov, O., Rossi, M., Boeck, T., 2010. Optimal linear growth in magnetohydrodynamic duct flow. J. Fluid Mech. 653, 273–299.

Lingwood, R., Alboussière, T., 1999. On the stability of the Hartmann layer. Phys. Fluids 11 (8), 2058–2068.

Moresco, P., Alboussière, T., 2004. Experimental study of the instability of the Hartmann layer. J. Fluid Mech. 504, 167–181.

Moser, R., Moin, P., 1987. The effects of curvature in wall-bounded turbulent flows. J. Fluid Mech. 175, 479–510.

Moureau V., Domingo P., Vervisch L., 2011. Design of a massively parallel CFD code for complex geometries. Comptes Rendus Mécanique. 339, 141–148.

Nagata, M., Kasagi, N., 2004. Spatio-temporal evolution of coherent vortices in wall turbulence with streamwise curvature. Journal of Turbulence 5 (17), 1–26.

Ni, M. J., Munipalli, R., Huang, P., Morley, N. B., Abdou, M. A., 2007a. A current density conservative scheme for incompressible MHD flows at a low magnetic reynolds number. Part II: On an arbitrary collocated mesh. J. Comput. Phys. 227 (1), 205–228.

Ni, M.-J., Munipalli, R., Morley, N. B., Huang, P., Abdou, M. A., 2007b. A current density conservative scheme for incompressible MHD flows at a low magnetic reynolds number. Part I: On rectangular collocated grid system. J. Comput. Phys. 221 (1), 174–204.

Reed, C. B., Picologlou, B. F., 1989. Sidewall flow instabilities in liquid metal flow under blanket relevant conditions. Fusion Technology 15, 705–715.

Roberts, P. H., 1967. An Introduction to Magnetohydrodynamics. American Elsevier Publishing Company, Inc. New York.

Tabeling, P., Chabrerie, J. P., 1981. Magnetohydrodynamic secondary flows at high hartmann number. J. Fluid Mech. 103 (225-239).

Thess, A., Zikanov, O., 2007. Transition from two-dimensional to three-dimensional magnetohydrodynamic turbulence. J. Fluid Mech. 579, 383–412.